



## City Research Online

### City, University of London Institutional Repository

---

**Citation:** Zakeri Nazar, Y., Askari, R. & Masdari, M. (2025). Utilisation of Insect-inspired Blades for Improvement of a Commercial Propeller Aerodynamic Performance. The Aeronautical Journal, 129(1341), pp. 3057-3082. doi: 10.1017/aer.2025.10041

This is the published version of the paper.

This version of the publication may differ from the final published version.

---

**Permanent repository link:** <https://openaccess.city.ac.uk/id/eprint/35230/>

**Link to published version:** <https://doi.org/10.1017/aer.2025.10041>

**Copyright:** City Research Online aims to make research outputs of City, University of London available to a wider audience. Copyright and Moral Rights remain with the author(s) and/or copyright holders. URLs from City Research Online may be freely distributed and linked to.

**Reuse:** Copies of full items can be used for personal research or study, educational, or not-for-profit purposes without prior permission or charge. Provided that the authors, title and full bibliographic details are credited, a hyperlink and/or URL is given for the original metadata page and the content is not changed in any way.


---

---



## RESEARCH ARTICLE

# Utilisation of insect-inspired blades for improvement of a commercial propeller aerodynamic performance

Y. Zakeri Nazar<sup>1</sup>, R. Askari<sup>1</sup>  and M. Masdari<sup>2</sup> 

<sup>1</sup>School of Aerospace Engineering, College of Interdisciplinary Science and Technology, University of Tehran, Tehran, Iran

<sup>2</sup>School of Science & Technology, Department of Engineering, City St George's University of London, London, UK

**Corresponding author:** M. Masdari; Email: [mehran.masdari@city.ac.uk](mailto:mehran.masdari@city.ac.uk)

**Received:** 9 December 2024; **Revised:** 23 May 2025; **Accepted:** 28 May 2025

**Keywords:** aerodynamic performance; insect-inspired; multi-rotor; numerical simulations; propeller

## Abstract

Bio-inspiration can be used to improve the aerodynamic performance of commercial multirotor propellers. In the present study, insect wings are used as a source of inspiration, and the effects of inspiration from insect's wing shape on the propeller performance—, especially this effect on parameters like thrust, torque, and propeller efficiency, are investigated. Six insect species have been selected as inspiration: Hemiptera, Orthoptera, Neuroptera, Mantodea, Odonata and Hymenoptera. The analyses have been done using the numerical simulation of flow and the moving reference frame (MRF) method alongside the SST  $k-\omega$  turbulence model. The simulations were carried out over a range of rotational speeds, varying from 4,000 to 8,000 rpm, for propellers with a diameter of 0.24 m. All propellers utilised the Eppler E63 airfoil. To ensure the accuracy of the present numerical simulation results, validation was done by comparing them with experimental data from the DJI Phantom-3 propeller. The results of validation showed significant agreement with the experimental data. The results indicated that the insect-inspired propellers generate higher thrust compared to conventional propellers. Additionally, for a constant thrust force, the inspired propellers exhibit lower rotational speeds. Moreover, in terms of thrust, the Hemiptera insect-inspired propeller outperforms the DJI Phantom-3 propeller, achieving a notable average improvement of 34.182%.

## Nomenclature

### Parameters

T	thrust
Q	torque
$\eta_P$	propeller efficiency
$P_m$	required mechanical power
$C_T$	thrust coefficient
$C_P$	power coefficient
$C_Q$	torque coefficient
n	rotational Speed
D	diameter

### Symbol Insect Species

Ma.	Mantodea
Ne.	Neuroptera
Or.	Orthoptera
Od.	Odonata
Hy.	Hymenoptera
He.	Hemiptera

## 1.0 Introduction

The commercial multi-rotors and their current popularity due to covering a wide range of applications and features is not hidden from anyone, especially due to their manoeuvrability, ability to hover and vertical take-off and landing (VTOL) capability. Therefore, the multi-rotors have been put in the civil applications such as environmental inspections, traffic monitoring, aerial surveying, pollution inspection, delivery and so on [1]. Today, multi-rotors are known as one of the important and reliable platforms of technology for the replacement and transformer of traditional and conventional methods into modern methods in various fields [2].

In commercial multi-rotor configurations, the propellers provide the lift force, which is called the thrust. For a small multi-rotor, the small dimensions of its propellers cause operating at low Reynolds numbers; it is often less than 100,000 [3]. This low Reynolds number effect make it more difficult to estimate the performance of small-scale propellers. In addition, with the small propeller scales, a relatively thick boundary layer is formed on the propellers, which increases the drag force and decreases lift-to-drag ratio [4]. Therefore, their small dimensions cause a reduction in performance at low Reynolds numbers, in which the viscous effects are dominant. These effects usually result in battery consumption, flight time reduction or decreasing limitation of payload that can be carried. In addition, considering the near-ground flight, one of the important concerns about the commercial multi-rotors is the noise produced by these multi-rotor configurations [5]. Despite using lithium batteries, propellers are still one of the main sources of noise [6, 7]. Therefore, more efforts should be made in the design of this component in order to improve flight time, payload and reduction of noise.

In 2003, Bohorquez et al. [8] experimentally studied the design, analysis and performance of the rotary wings hover in micro aerial vehicles (MAVs). The results showed that one of the aerodynamic weaknesses was the inappropriate choice of planform. In 2007, Ramasamy et al. [9] experimentally investigated the flow field of the rotary wing in MAVs and showed the important role of increasing the boundary layer thickness and turbulence effects in reducing aerodynamic efficiency. Brandt and Selig [10], in 2011, experimentally studied the effects of propeller diameter and number of propellers on the unmanned aerial vehicle UAV performance. Jordan et al. [11], in 2020, experimentally investigated the performance of commercial multi-rotor's propellers for the purpose of development and validation. Their results showed that the overall sound pressure level with low harmonics are increased as the rotational speed increases. The results of the numerical studies conducted by Shams-uddin and Madzni [12] in 2021 on the configuration of the rotors showed that the optimal design of the propellers and the configuration of the rotors is important to improve the aerodynamic performance and the efficiency of the propulsion system. Deters et al. [13], in 2017, experimentally investigated the static performance of the propellers and engines of small multi-rotor configurations. Their results confirmed the flight time reported by the manufacturer and created a data bank of propeller performance data. Hintz et al. [14], in 2018, experimentally investigated the effects of the insect-inspired planform of cicada wings on thrust and energy consumption, and their results showed that this bio-inspired propeller improves the efficiency.

The first researches on bio-inspired propellers were carried out numerically in 2014 by Gomez et al. [15], in which the cicada wing was selected to study. Their results showed that bio-inspired propellers create weaker vortices and are more eligible for using in rotor-crafts. In 2017, Ning and Hu [16] experimentally studied the aerodynamic and aero-acoustic characteristics of multi-rotor propellers inspired by a combined shape of cicada wings and maple seeds. They showed that for the same input power, it can produce the same thrust using a conventional propeller for a lower RPM at the hovering operating condition.

In 2018, Ikeda et al. [17] conducted their experimental studies on the effects of leading-edge serrations on aerodynamic force production using a single-feather, clean, serration wing inspired by an owl. In these studies, the size and spacing of the leading-edge serrations were done using the particle image velocimetry (PIV) methods and force measurements.

Wei et al. [18] conducted a comparative study using computational fluid dynamics (CFD) methods and rotation tests on the leading edge teeth inspired by the owl wing with different morphologies in

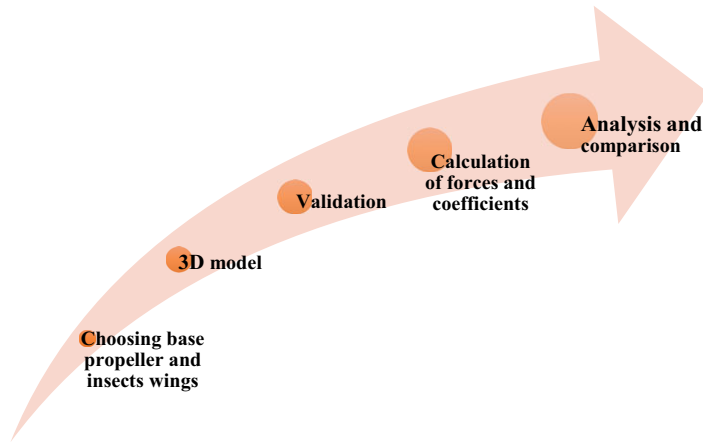


**Figure 1.** *Process of this research.*

order to evaluate their effects on reducing noise and increasing thrust force. Their results showed that the owl wing inspiration is useful for aerodynamic control and increasing aerodynamic performance in the design of blades.

In 2022, Masdari et al. [19] conducted an experimental study on the acoustic properties of propellers modeled after insect wings from five different species and a plant seed. Their bio-inspired propellers demonstrated superior thrust and rotation at lower speeds, while also producing less noise compared to the baseline propeller.

In 2022, Moslem et al. [20] also experimentally focused on the acoustic characteristics of five insect-inspired propellers and a plant seed-inspired propeller. They showed that their bio-inspired propellers have better thrust and rotate at lower rotational speed, and they also created a lower noise level than the baseline propeller.

By reviewing the studies and research done in the field of using the method of bio-inspiration, especially the inspiration from insect wings, the limitations of this research can be understood. Most of the research has been focused on the aeroacoustics of a limited insect-inspired propellers. Focusing on the aerodynamics of propellers, this research has explored a greater and more diverse number of insect wings for inspiration. Unlike most research that used experimental methods, the numerical methods have been used in this research to simulate the flow field around the propellers and calculate the aerodynamic characteristics. The primary objective is to enhance the aerodynamic performance of propellers and explore the potential of using bio-inspired propellers as an alternative to conventional propellers.

The research procedures are illustrated and present in Fig. 1 to give an aspect. Each of the steps in this figure is fully explained in the following sections.

## 2.0 Multi-rotor's geometrical and performance parameters

Their cross-sections of propellers are aerofoils that are placed uniformly in the spanwise direction, as in Fig. 2(a). Thus, the propeller blades have geometric characteristics similar to aerofoils, including the trailing edge, leading edge, chord, thickness and more, as depicted in Fig. 2(b) [21, 22]. The number of blades of a multi-rotor can vary based on its design consideration. They typically utilise two blades for stability, control and overall weight consistency of the structure [23]. The geometric pitch or theoretical pitch, actual or effective pitch, and twist angle known as pitch angle are illustrated in Fig. 2 and described in Refs (21 and 22).

One of the parameters that can be used for the performance of the propeller is the propeller efficiency, which can be calculated from the relation (Equation(1)) and is defined as the ratio of the output power

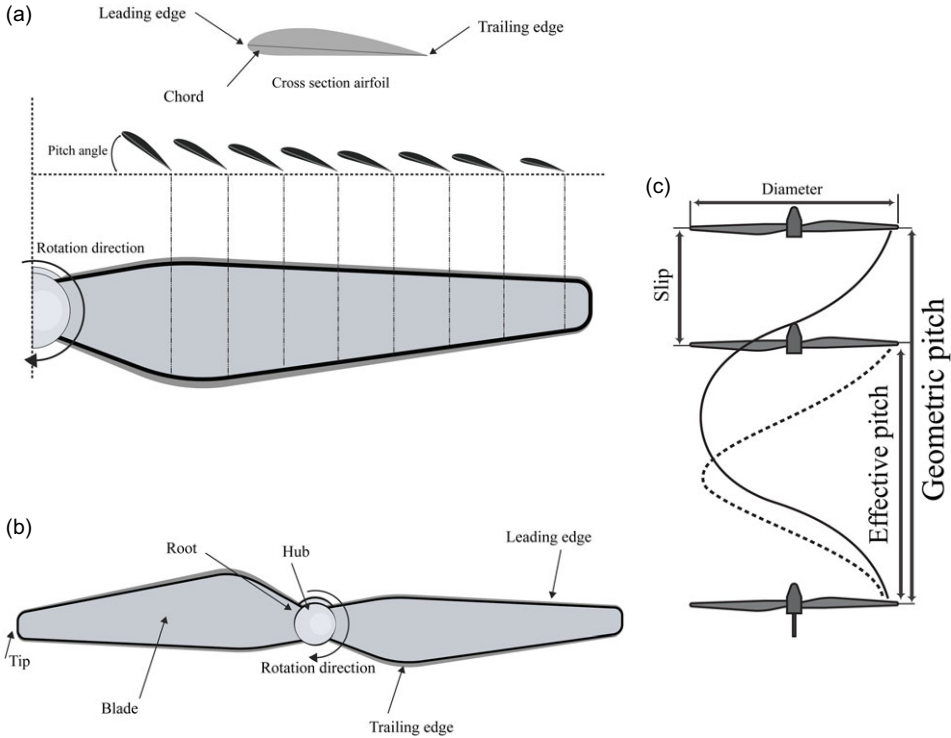


**Figure 2.** Propeller geometry and performance parameter; propeller cross-section at different local radius and twist along the span (a); propeller's geometry parameter (b); geometric pitch, effective pitch and advance ratio (c).

(which is the driving power) to the input power (which is the mechanical power) [13].

$$\eta_p = \frac{TV_0}{P_m} \quad (1)$$

where  $T$  is the thrust,  $V_0$  is the free-stream velocity and  $P_m$  is the required mechanical power, which can be calculated from the following relation [13]:

$$P_m = 2\pi nQ \quad (2)$$

where  $Q$  is the torque and  $n$  is the rotational speed (in rpm). In the propeller efficiency equation,  $C_p$  is the power coefficient and  $C_T$  is the thrust coefficient, which can be calculated from the following relations [13]:

$$C_T = \frac{T}{\rho n^2 D^4} \quad (3)$$

$$C_p = \frac{P_m}{\rho^3 D^5} \quad (4)$$

Also, the torque coefficient,  $C_Q$ , can be defined as the following relation [24].

$$C_Q = \frac{Q}{\rho n^2 D^5} \quad (5)$$

In the above relations,  $\rho$  is the flow density and  $D$  is the propeller diameter. The advance ratio,  $J$ , is calculated from the relation (Equation (6)). Due to the low value of the speed, the advanced ratio in this

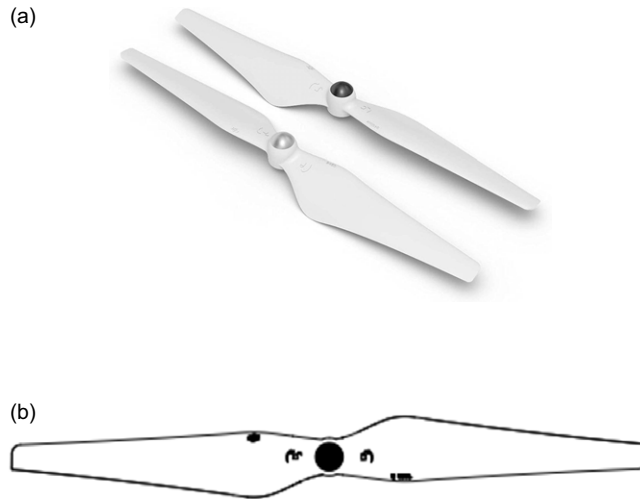


**Figure 3.** Image of DJI Phantom-3 propeller (a), and its schematic (b) [26].

research is very close to zero [24].

$$J = \frac{V_0}{nD}. \quad (6)$$

Using Equations (1) to (4) and Equation (5), another relation for the propeller efficiency could be obtained:

$$\eta_P = J \frac{C_T}{C_P} \quad (7)$$

### 3.0 Geometry of insect-inspired propeller

Regarding the experimental test that has been done on DJI phantom-3 propeller in Ref. (13) and the existence of the experimental data, it is a suitable choice to consider as the base propeller for the present study, in order to validate the numerical simulation. This propeller has diameter of 0.24 m [25] as shown in Fig. 3.

Selecting the wings of insects was a significant challenge in this research. One of the key requirements is the availability of a perfectly captured wing planform. In other words, a high-quality image from a top view that accurately depicts the final shape of the wing's planform is necessary. However, obtaining such an image is difficult due to various factors. Many insects have extremely small dimensions, rapid movement and unique rest positions of wings, making it rare to find high-quality images that showcase the planform characteristics and features. This issue has been a fundamental challenge in choosing insect wings. For this reason, insects with these characteristics have been excluded due to the lack of suitable images. Consequently, this scarcity of suitable images adds to the challenge of wing selection. In the selection process of insect wings, one crucial factor to consider is the simplicity of the borderlines that define its shape. This holds particularly true when utilising design software for three-dimensional modeling, and depends on the level of expertise involved.

Figure 4 is a summarised classification of winged insects. Winged insects are divided into two parts: Paleoptera and Neoptera. Paleoptera, like dragonflies, do not have the ability to fold their wings, whereas Neoptera show this ability and are divided into two parts: exopterygota and endopterygota. Among the insects classified in Fig. 4, considering some concerns including the availability of images to use for the initial steps of modeling, some specific features of the species, and clarity of available images, several species from the chart in Fig. 4 have been chosen for further studies. Figure 5 is designed and illustrated in order to show the family order of insect and that special insect whose wings are selected.

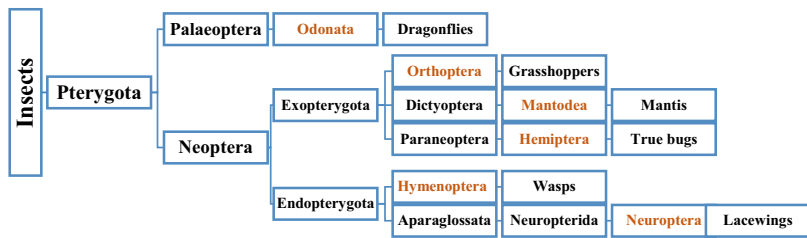


*Figure 4. Insect's family chart [40].*

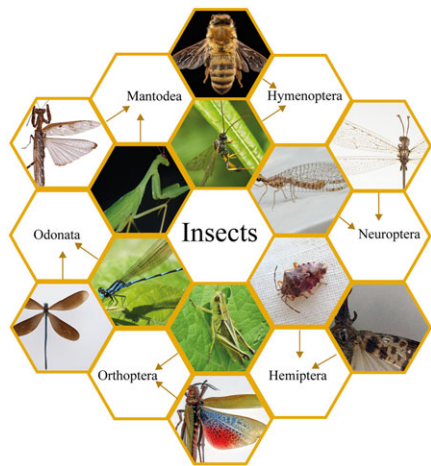


*Figure 5. Selected insect's species for capturing their wings [40].*

In the internal cells of this graph the insects are related to the family shown and in the external cells are that special insect whose wings are selected are illustrated. In the centre of Fig. 5, six selected insect species are placed. These selected species belong to the Hemiptera, Orthoptera, Neuroptera, Hymenoptera, Mantodea and Odonata. Odonata has more than 6000 species and is divided into two subcategories of dragonflies and mayflies [27]. Although they are different in appearance, dimensions and the way the wings are positioned in the resting phase, all Odonata species have a pair of forewings and a pair of hindwings. The other selected wing is from the Hemiptera family order, which has more than 80,000 known species. Aphids and field crickets are some examples of this order. Usually there are wings in Hemiptera, however, some of them are wingless or lose their wings. Neuroptera is an order of insects with about 6000 known species. Silky wings and spoon wings are examples of Neuroptera. Their dimensions vary from small to large, with a wing length of more than 100 mm [28, 29]. Neuroptera usually have four large, membranous and unequal wings, and when resting, the wings are placed behind the insects like a tent [29]. Mantodea has more than 2400 species. It is the next selected insect family order for inspiration. Mantises are the largest family of this order. The size of wings in mantises can be big or small, or there are no wings at all. If there are wings, mantises have two pairs of wings. Orthoptera is an order of insects with about 20,000 to 250,000 known species. This order of insects includes crickets and grasshoppers. These insects do not have the ability to fold their wings while resting, thus the wings are tangent to the body. Hymenoptera is one of the largest orders of insect. More than 120,000 species of these insects are known. Hymenoptera usually have two pairs of wings, and the forewings are larger than the hindwings. Bees and ants are insects of this order.

The selection of each insect and the reason for this selection was one of the most important and challenging parts of this research. One of the most important activities carried out in this regard was the review of previous related studies as we talked about in the last review [20], insect wings have



special aerodynamic qualities that help them fly higher and quieter. Accordingly, and based on previous studies and investigations, there was a need to investigate aerodynamic performance in the continuation of research and studies conducted in this field. Therefore, we included families of insects that had been previously investigated in the review list. In addition, as an innovation, insects from new families were also selected, the results of which indicate their good performance. Some insects such as Orthoptera and Mantodea have not been studied before, and the reason for choosing these insects is to expand more references for inspiration in this field.

- **Odonata:**

The insect selected from the dragonfly species is “**Matrona Basilaris**”. One of the main reasons for choosing this wing is the multiplicity of studies that have been done on dragonflies from various aspects such as wing structure and behaviour, section, flight and aerodynamics [26–35]. Also, the planform of these wings, especially the shape of the leading edge, is simple and is a suitable choice for three-dimensional modeling.

- **Hymenoptera:**

The next selected wing is from the Hymenoptera species, which many studies on the flight and wing of this species has been done [38, 39]. The insect selected from this species with the scientific name “**Apis mellifera**” is a honey bee. It is one of the fastest flying insects that has a simple planform line and shape.

- **Neuroptera:**

The wing of the “**Creoleon prolongaveruntus**” insect from the Neuroptera species is the third selected wing. In general, the insects of this species are similar in appearance to a suborder of dragonflies in Odonata family, and the wing of the selected insect is almost similar to the wings of dragonflies, with the difference that its width is less. Also, its simple shape and planform line is one of the main reasons for choosing this wing.

- **Hemiptera:**

The wing of the “**pyrops clavatus**” insect from Hemiptera has been chosen as the fourth wing because it has a large wing surface and a simple planform line.

- **Orthoptera and Mantodea:**

There is no research on the wings of Orthoptera species and Mantodea and is the reason for choosing the insects “**Phymateus karschi**” and “**Raptrix perspicua**” from these species. In addition to simple shape and similar planform line to other selected wings, there is an interest to investigate their wing potential for inspiration in modeling for use in small multi-rotor interiors.

To create a precise three-dimensional model of a propeller blade, it is crucial to determine three essential factors: the chord distribution, twist distribution and aerofoil of the propeller section. To achieve the geometrical properties for each insect, its right forewing was selected. Considering the top view of each insect wing, the closed curve that includes the perimeter of the wing and defines the general shape of the wing has drawn accurately, similar to Fig. 6. This closed curve is the wing planform. However, it should be noted that insect wings like that shown in Fig. 6 may have some broken or torn parts on the leading or trailing edge, which for making modeling easier, these parts are not considered during the drawing of the planform curve, like what is shown in Fig. 6 from a closer view (see red circle).

To ensure a fair comparison, all insect-inspired propellers needed to be scaled and dimensionless proportionately to the base propeller radius, as depicted in Fig. 7(a). The planform curves drawn in the previous step are placed in a grid. Therefore, for all insect wings, their tips are exactly located at the position of  $r/R$  equal to 1 of grid, and their roots are located at the position of  $r/R$  equal to 0 of grid. For the simulations that will be explained in the next section, by scaling, all wings have a radius of 0.12 m, similar to the base propeller. Once the scaling of the insect-inspired propellers was accomplished, the chord at each  $r/R$  (radius ratio) could be obtained from the chord distributions shown in Fig. 7. Further description regarding the modeling of the present insect-inspired propellers is presented in Refs (40 and 41).

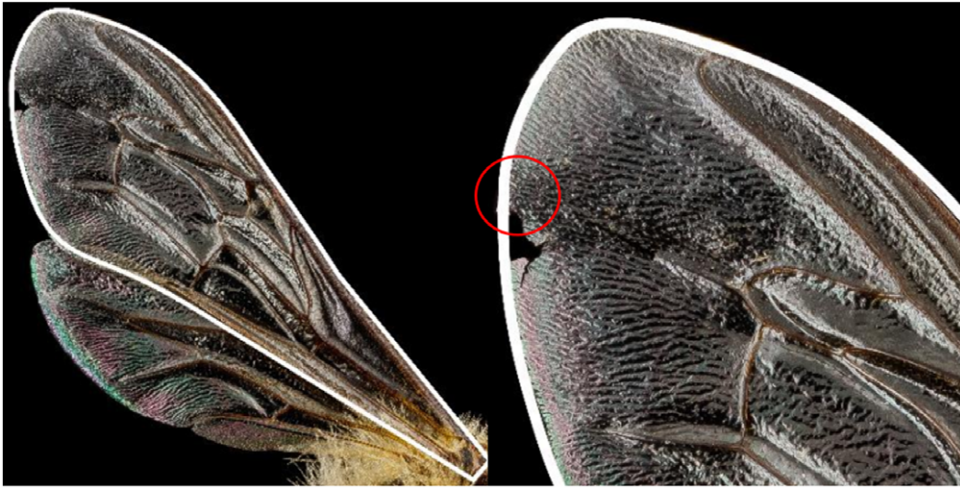


**Figure 6.** The process of wing planform capturing, in a case, facing with scratches on the edge of the wing of Hemiptera.

The three-dimensional geometry modeling of the propellers was executed using SolidWorks software, incorporating specific twist and chord values for each section's aerofoil. After merging the sections, the final solid geometries of the propellers were obtained, as depicted in Fig. 8. It should be acknowledged that the mentioned three-dimensional modeling of the insect wings may contain some modeling errors and simplifications. However, these would only yield a negligible margin of error. The twist distribution, taking into account previous studies [13, 20], starts at 17.72 degrees from the root to approximately 30% of the propeller radius. From that point to the tip, the twist decreases linearly to 4.7 degrees. Since there is a lack of information regarding the geometry and aerofoil specifications of the DJI Phantom-3, EPPLER E63 aerofoil, shown in Fig. 7(h), is considered for our insect-inspired propellers. This aerofoil is widely used in research on small-scale propellers and is known to be a suitable choice for low Reynolds number flows [16, 20]. This aerofoil is utilised for all sections and propellers in this study. For three-dimensional modeling of other propellers, the diameter is hold fixed, equal to the base propeller. Also, considering that the geometry of the hub does not have a significant effect on the results of this research, the hub shape is considered constant for all propellers.

#### 4.0 Numerical simulation methodology and validation

The governing equations of fluid dynamics include the continuity equation, momentum equation and energy equation, which are given below and are fully explained in Refs (47–49).

##### 1. Continuity equation or law of conservation of mass:

Equation (8) is general and used in compressible and incompressible fluids [47].

$$\frac{\partial \rho}{\partial t} + \nabla \cdot (\rho \vec{V}) = 0. \quad (8)$$

##### 2. The momentum equation

The momentum equation can be written in three directions – x, y, z – and is available in Ref. (47).

$$\rho \left[ \frac{\partial \vec{V}}{\partial t} + (\vec{V} \cdot \nabla) \vec{V} \right] = -\nabla p + \nabla \cdot \bar{\bar{\tau}} + \rho \vec{f}. \quad (9)$$

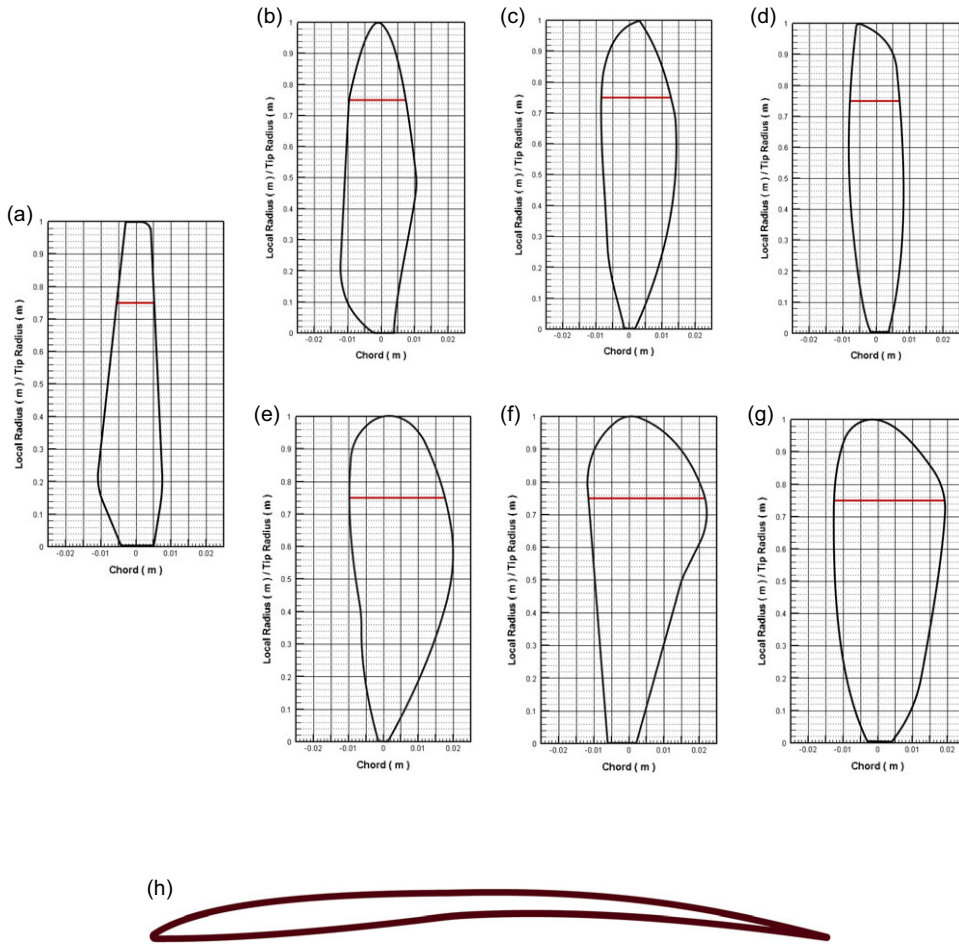


**Figure 7.** Schematic of: base propeller (a), Mantodea (b), Neuroptera (c), Orthoptera (d), Odonata (e), Hymenoptera (f), Hemiptera (g), Eppler E63 aerofoil (h).

The second term on the right side of Equation (2) is the viscous stress tensor, and the third term on this side is the body forces. The viscous stress tensor is given in Equation (10) [48].

$$\tau_{ij} = \mu \left( \frac{\partial V_i}{\partial x_j} + \frac{\partial V_j}{\partial x_i} \right) + \lambda (\nabla \cdot \vec{V}) \delta_{ij}. \quad (10)$$

And  $\delta_{ij}$  which is called Kronecker delta.

### 3. The energy equation

The third equation is the energy equation, which was not calculated in this study and its equation is fully presented in the Ref. (47).

### Governing equation

The general form of Navier-Stokes equations is as Equation (11), and the new terms appearing in this equation are turbulence effects. To solve this equation, the Reynolds stresses in the third term on the right should be modeled [49].

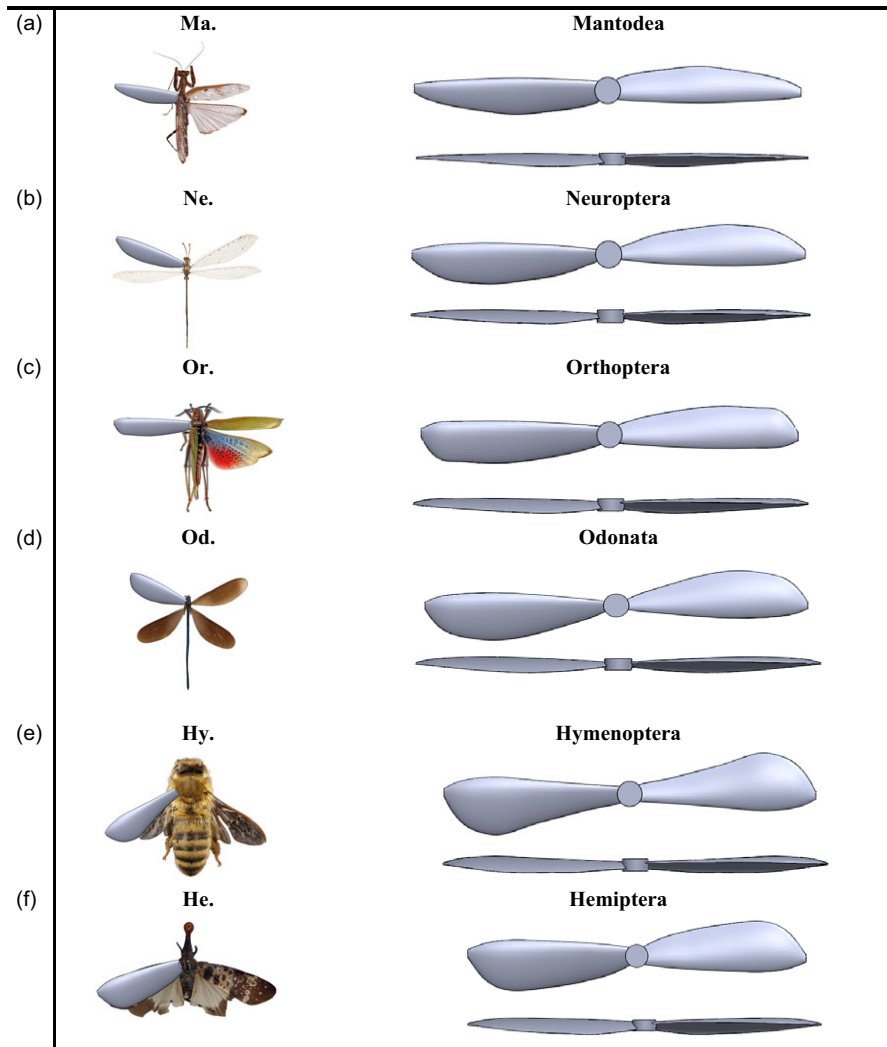


**Figure 8.** Three-dimensional models of bio-inspired propellers, Mantodea (a) [42], Neuroptera (b) [43], Orthoptera (c) [44], Odonata (d) [45], Hymenoptera (e), Hemiptera (f) [46].

$$\begin{aligned} \frac{\partial}{\partial t}(\rho u_i) + \frac{\partial}{\partial x_j}(\rho u_i u_j) = & \\ -\frac{\partial p}{\partial x_i} + \frac{\partial}{\partial x_j} \left[ \mu \left( \frac{\partial u_i}{\partial x_j} + \frac{\partial u_j}{\partial x_i} - \frac{2}{3} \delta_{ij} \frac{\partial u_i}{\partial x_i} \right) \right] & \\ + \frac{\partial}{\partial x_j} (-\rho \overline{u'_i u'_j}) & \end{aligned} \quad (11)$$

The general form of the instantaneous Navier-Stokes equations is as Equation (3), and the new terms appearing in this equation are turbulence effects. To solve this equation, the Reynolds stresses in the third term on the right should be modeled [49].

The flow field around the propellers are simulated numerically using ANSYS FLUENT and Multiple Reference Frame (MRF) method. MRF is a suitable method when there is a rotating section, like propeller, and the flow around this part is desired to simulate [50]. Noting the recommendation of the MRF method in previous studies [51–53] and also considering the subject of the current study, MRF method is

Table 1. Static domain independency

		Number of		Thrust(N)-	Thrust(N)-	Differences with	
	RPM	Elements	Dimensions	CFD	Deter's	Previous Num.	Differences
					Studies (13)	Case	with Exp.
2	8,000	880,745	H = 10D Dsd = 4D	6.78	6.93		0.0216
3	8,000	949,661	H = 14D Dsd = 4.41D	6.81	6.93	0.0044	0.0173

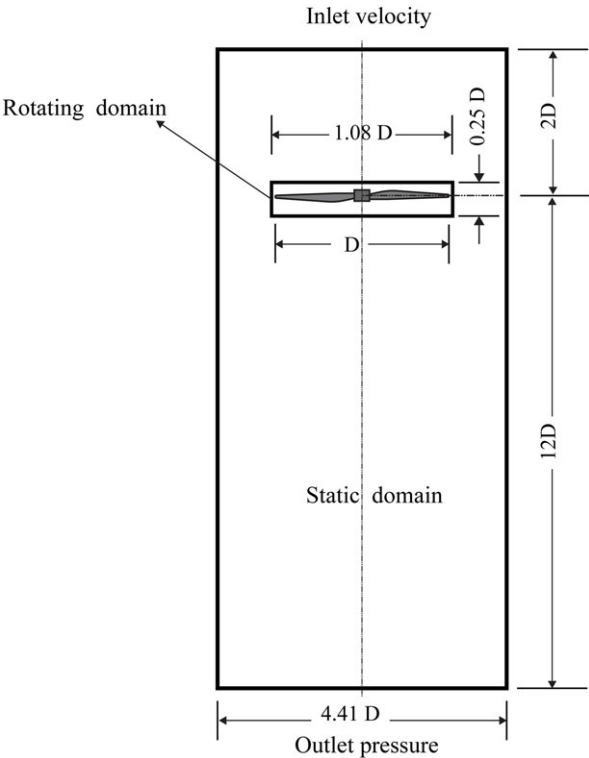


Figure 9. Computational domains along with dimensions and boundary conditions.

selected. Figure 9 illustrates the geometry of the computational domain that contains two parts: the rotating domain, which encloses the propeller, and the larger stationary domain, which includes the rotating domain. Design Modeler is used for the generation of this geometry. The propeller is fully enclosed within the rotating domain, causing the propeller tips to be slightly distanced from the interface. To enhance accuracy, two cases of different static domain dimensions were considered and the results were compared with experimental data conducted by Deters et al., as presented in Table 1. As a final step, by considering a compromise between the available computing resources, the number of simulation cases and the computational cost of each case by increasing  $H = 14D$  and  $Dsd = 4.41$ , it was observed that the thrust is obtained with less than 0.005 difference compared with the previous case ( $H = 10D$  and  $Dsd = 4$ ). Consequently, the diameter of the rotating domain is 1.08 times the propeller's diameter. On the other hand, the diameter and the height of the stationary domain cylinder is 4.14 times and 14 times the propeller's diameter, respectively [22, 51, 54].

For meshing of propeller and computational domain, ANSYS meshing was used. Considering the relatively small dimensions and the three-dimensional nature of the propeller, unstructured mesh and



**Table 2.** *Boundary conditions*

Domain	Boundaries	
Rotating Domain	Boundary-contact region	
	Type	Interface
	Location	contact region
	Boundary-propeller	
	Type	Wall
	Location	Propeller
Static Domain	Boundary-contact region	
	Type	Interface
	Location	contact region
	Boundary-inlet	
	Type	Velocity-inlet
	Location	Inlet
	Boundary-outlet	
	Type	Pressure-outlet
	Location	Outlet

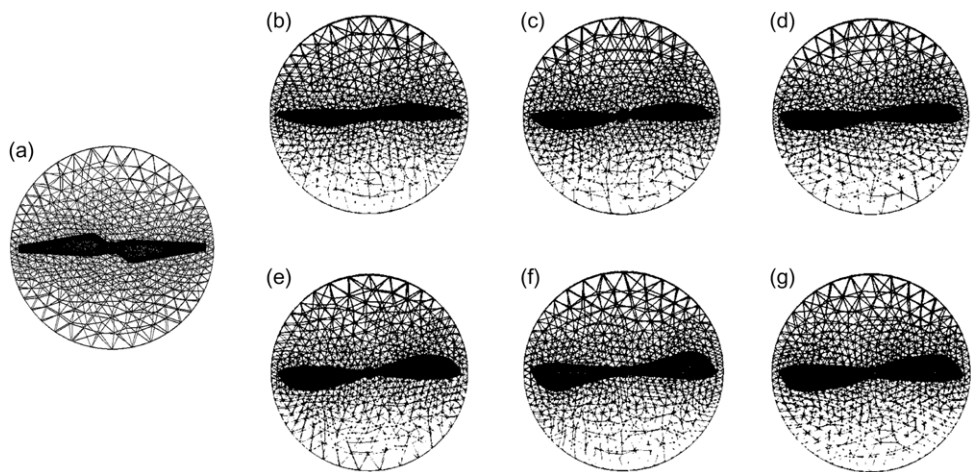


**Figure 10.** *Mesh of base propeller (a), Mantodea (b), Neuroptera (c), Orthoptera (d), Odonata (e), Hymenoptera (f), Hemiptera (g).*

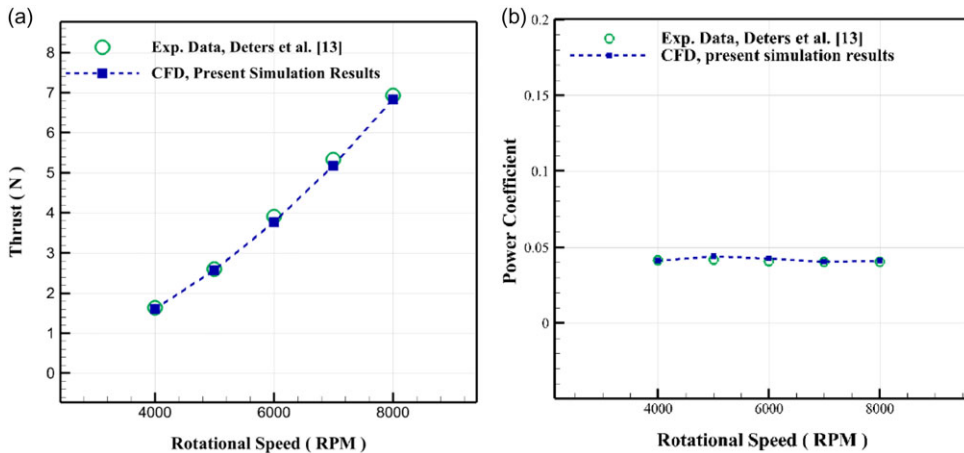
tetrahedral elements were utilised. Additionally, as viscosity effects were found to be predominant, boundary layer meshing and prism elements were employed. The calculations for Reynolds number and thickness of the turbulent boundary layer were conducted based on the chord and tangential speed at 75% of the propeller radius and standard temperature (see red lines at the insect’s wing planforms in Fig. 7) [3, 55]. Figure 10 presents the propeller’s mesh.

The boundary conditions between the rotation and stationary domains are defined and mentioned in Table 2. The turbulence intensity is considered 0.1 %, which is equivalent to the conditions available in the experimental condition whose data used in the present study [13]. Pressure outlet is chosen for its better convergence rate. The rotational speed is considered in the range of 4000 to 8000 rpm with a step of 1000 rpm.

The SST K- $\omega$  turbulence model is used for turbulence flow modeling in the present study. This model has been recommended and used by various researchers to analyse the aerodynamic performance of small propellers [5, 50, 55, 56]. Its governing equations represented below, and assumptions and constants are presented in these Refs (57, 58).

**Table 3.** Solution setting, numerical method and boundary conditions

Feature	Method/Boundary Condition
Solver	3D Pressure based
Turbulence model	k- $\omega$ SST model
Algorithm	Coupled
Discretisation	Second upwind scheme
Inlet boundary condition	Velocity inlet
Outlet boundary condition	Pressure outlet

**Figure 11.** Validation of numerical method, thrust versus RPM and power coefficient versus RPM.

$$\frac{\partial k}{\partial t} + U_j \frac{\partial k}{\partial x_j} = P_k - \beta^* k \omega + \left[ (v + \sigma_k v_T) \frac{\partial k}{\partial x_j} \right], \quad (12)$$

$$\frac{\partial \omega}{\partial t} + U_j \frac{\partial \omega}{\partial x_j} = \alpha S^2 - \beta \omega^2 + \frac{\partial}{\partial x_j} \left[ (v + \sigma_k v_T) \frac{\partial \omega}{\partial x_j} \right]. \quad (13)$$

Although there are higher computational costs with boundary layer meshing, this turbulence model is suitable for accurately modeling propeller turbulence. Typically, the average  $Y^+$  value is remained around one for all simulations. The solver for solution is pressure based with coupled algorithm and discretisation of all equations are based on second upwind scheme. Also for gradients, Least Squares Cell-Based is used. The solution settings and boundary conditions are summarised in Table 3. The solution process is repeated until the residuals reach the selected convergence criterion of 0.0001. Moreover, a convergence criterion of 0.0001 is also applied to the thrust and torque measurements. The number of iteration steps varies between 2000 and 3000.

## 5.0 Results and discussion

All propellers, including the base propeller and insect-inspired propellers, are numerically simulated according to the numerical model as was described in Section 4. At the following, the results of these simulations are presented. Figures 11(a) and (b) demonstrate the comparison of the thrust and power coefficient trends at various rotational speeds between the base propeller's numerical results obtained in the present study and the experimental results conducted by Deters et al. [13]. The results indicate a good agreement, representing the high accuracy of the present numerical simulation method. This

**Table 4.** *The rotational component of velocity for all insect-inspired propellers*

Rpm	R (m)	$r = 0.75R$	Velocity (m/s)
4,000	0.12	$r = 0.75R$	37.69
5,000	0.12	$r = 0.75R$	47.12
6,000	0.12	$r = 0.75R$	56.54
7,000	0.12	$r = 0.75R$	65.97
8,000	0.12	$r = 0.75R$	75.39

result suggests that the selected solution methodology is suitable for other bio-inspired propellers as well. However, it is important to note that there are some small differences between the experimental and numerical results because of various factors. One of the main reasons is that there is no access to precise geometric information of the DJI Phantom-3 propellers provided by Manufacturer Company, including the chord distribution, twist and cross-section aerofoil. The geometric information of the propellers in Deter’s studies are also using propeller scanners [13]. This may introduce errors in the modelling of base propeller and analysis. In order to compensate for this, the chord distribution and twist were determined based on previous studies [13, 20], which may slightly differ from the original propeller geometry used in the experimental. Moreover, the exact aerofoil of the DJI Phantom-3 propeller is unknown, so the EPPLER E63 aerofoil was chosen for the cross-section in the numerical simulations. This discrepancy in airfoil selection can also contribute to the disparity between the results obtained from the two methods.

Figures 12(a)–(g) present the pressure distribution contours on both the upper and lower surfaces of the base and bio-inspired propellers, at an average rotational speed of 6000 rpm. It can be seen in these pressure contours, as expected, the static pressure of the pressure surface is higher than the suction surface, resulting in an upward force known as lift which is called thrust force in propoulsion terminology. This force is responsible for the upward movement of drones and is generated by the propeller’s blades. The magnitude of this thrust is directly proportional to the pressure difference between the two surfaces.

Considering a fixed rotational speed, the velocity magnitude experienced by the leading edge of the airfoil at each span-wise blade increases as the radius of its section increases. Therefore, there is a reduction in pressure from the root to the tip of the blades, as is evident by the span-wise pressure distribution in these contours (Figs 12(a)–(g)). In addition, the contours of velocity magnitude (Figs 13(a)–(g)) and streamlines (Figs 14(a)–(g)) are shown in the following to provide comprehensive physical information about the flow filed created by these inspect-inspired propellers in comparison with the base propeller.

The velocity contours and streamlines were showed in Figs 13 and 14, respectively. These figures develop numerical results at a rotational speed of 6000 for all insect-inspired propellers.

Also, the propeller rotational speed at a local radius of 0.75R is calculated for all rotational speeds in Table 4.

Figure 15 illustrates that as the rotational speed increases from 4000 to 8000 rpm, there is a noticeable increase in the thrust for all bio-inspired propellers, as is expected, similar to what is observed for the base propeller. An important finding is that the rate at which the thrust force changes due to an increase in rotational speed varies among the propellers and significantly depends on their blade shapes. The value of thrust change resulting from variations in rotational speed: for the base propeller, it ranges from 1.60 to 6.83 Newton; for Mantodea, it ranges from 1.56 to 6.62 Newton; for Neuroptera, it ranges from 1.80 to 7.59 Newton; for Orthoptera, it ranges from 2 to 8.38 Newton; for Odonata, it ranges from 2.14 to 8.89 Newton; for Hymenoptera, it ranges from 2.24 to 9.34 Newton; and for Hemiptera, it ranges from 2.28 to 9.45 Newton. Consequently, most bio-inspired propellers have a greater thrust than the DJI Phantom-3 propeller. Among the propellers examined in this study, Hemiptera demonstrates the highest rate of thrust change so that at the rotational speed of 8000 rpm, it produces a thrust value that is 36.21% higher than that of the DJI Phantom-3 propeller. The Mantodea propeller closely aligns with the base propeller’s thrust pattern as the rotational speed increases. In between, Orthoptera and Neuroptera exhibit a moderate behaviour.



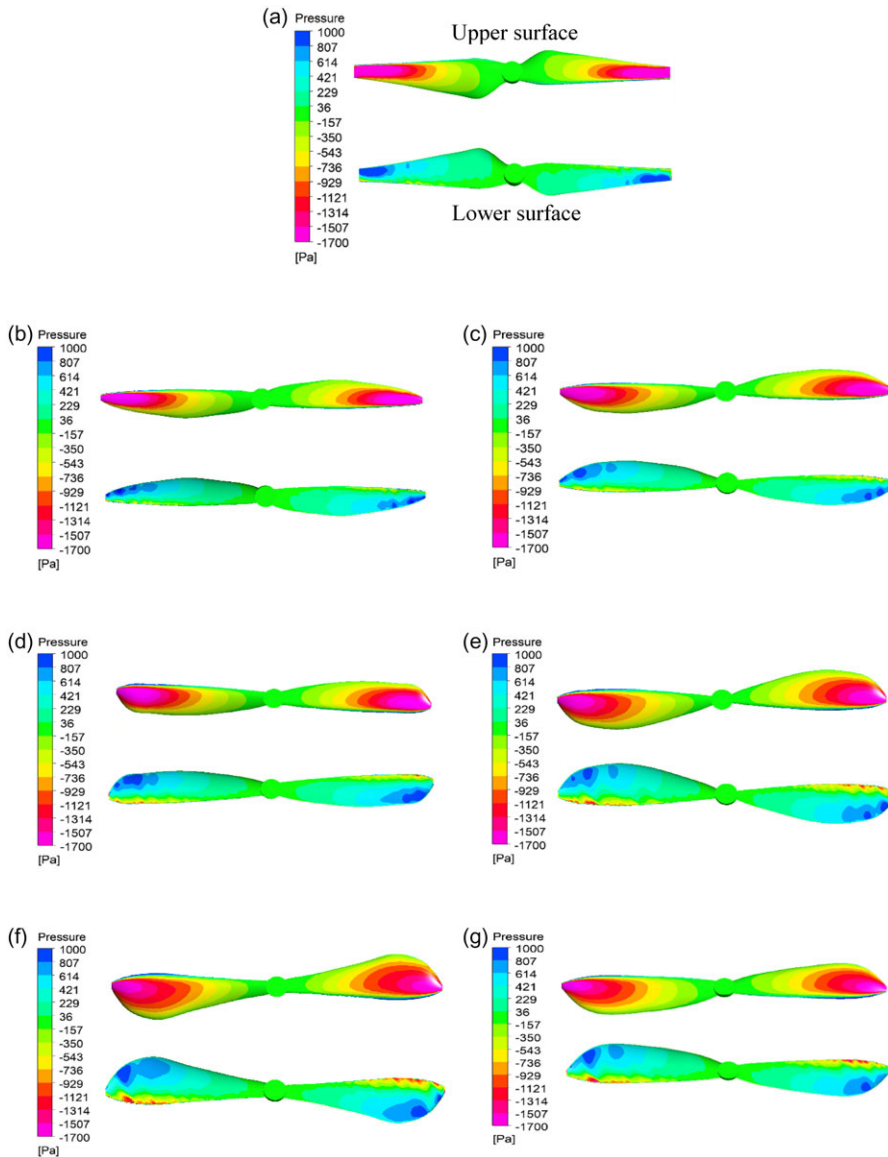


**Figure 12.** Pressure contour of base propeller (a), Mantodea (b), Neuroptera (c), Orthoptera (d), Odonata (e), Hymenoptera (f), Hemiptera (g).

In Fig. 16, the changes in the thrust coefficient are depicted as the rotational speed varies. It is apparent that the thrust coefficient also experiences a slight increase as the rotational speed is raised. Similarly, to the trend observed in the thrust values of the propellers, the bio-inspired propellers generally exhibit higher thrust coefficient values. Specifically, the Hemiptera-inspired propeller demonstrates the highest thrust coefficient values across all rotational speeds. The Mantodea-inspired propeller is similar to the base propeller. Once again, it is noted that the propellers inspired by Orthoptera and Neuroptera exhibit a moderate behaviour. It also needs to mention that in for a fixed reference area (disk area), the increase in thrust is due to a combined effect of the planform shape and the blade surface, which, of course, the planform alone (and without taking into account the concerns including weight, construction and structure) are not considered a definite advantage.

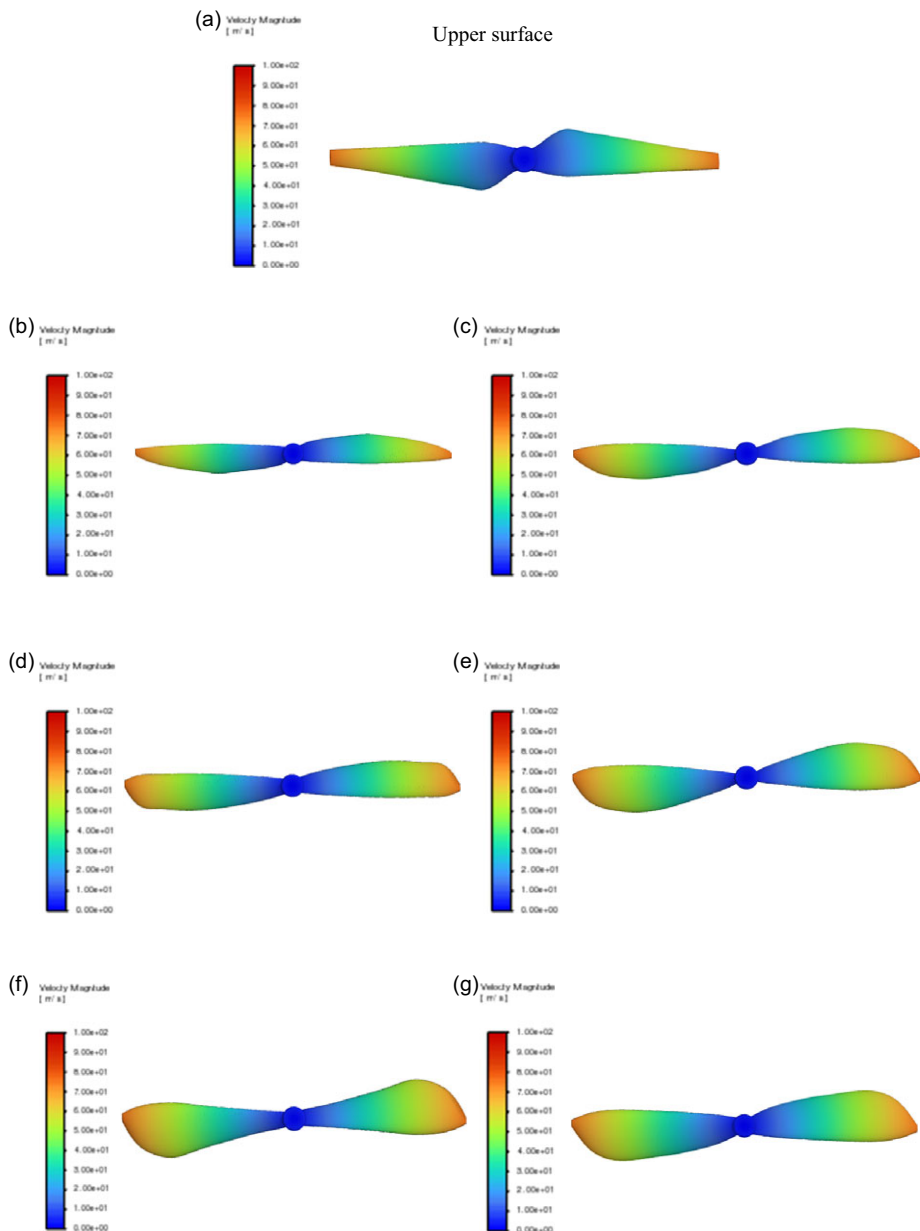


**Figure 13.** Velocity magnitude contours of base propeller (a), Mantodea (b), Neuroptera (c), Orthoptera (d), Odonata (e), Hymenoptera (f), Hemiptera (g).

Figure 17 shows the mechanical power required to rotate the propellers. This power is calculated using Equation (2). The calculation takes into account the torque value obtained from the simulation results. Figure 17 displays the torque coefficient for various propellers at different rotational speeds, as determined using Equation (7). Considering Figs 17 and 18, it is seen that as the rotational speed increases, the propeller's torque and consequently the mechanical power also increase. Additionally, propellers with wider chord distributions require more mechanical power to rotate, which can lead to increased noise and drag. This trend is evident in the Hymenoptera, Odonata, and Hemiptera. In contrast, the Mantodea and Neuroptera propellers, with their relatively narrower chord distributions, show consistently lower values

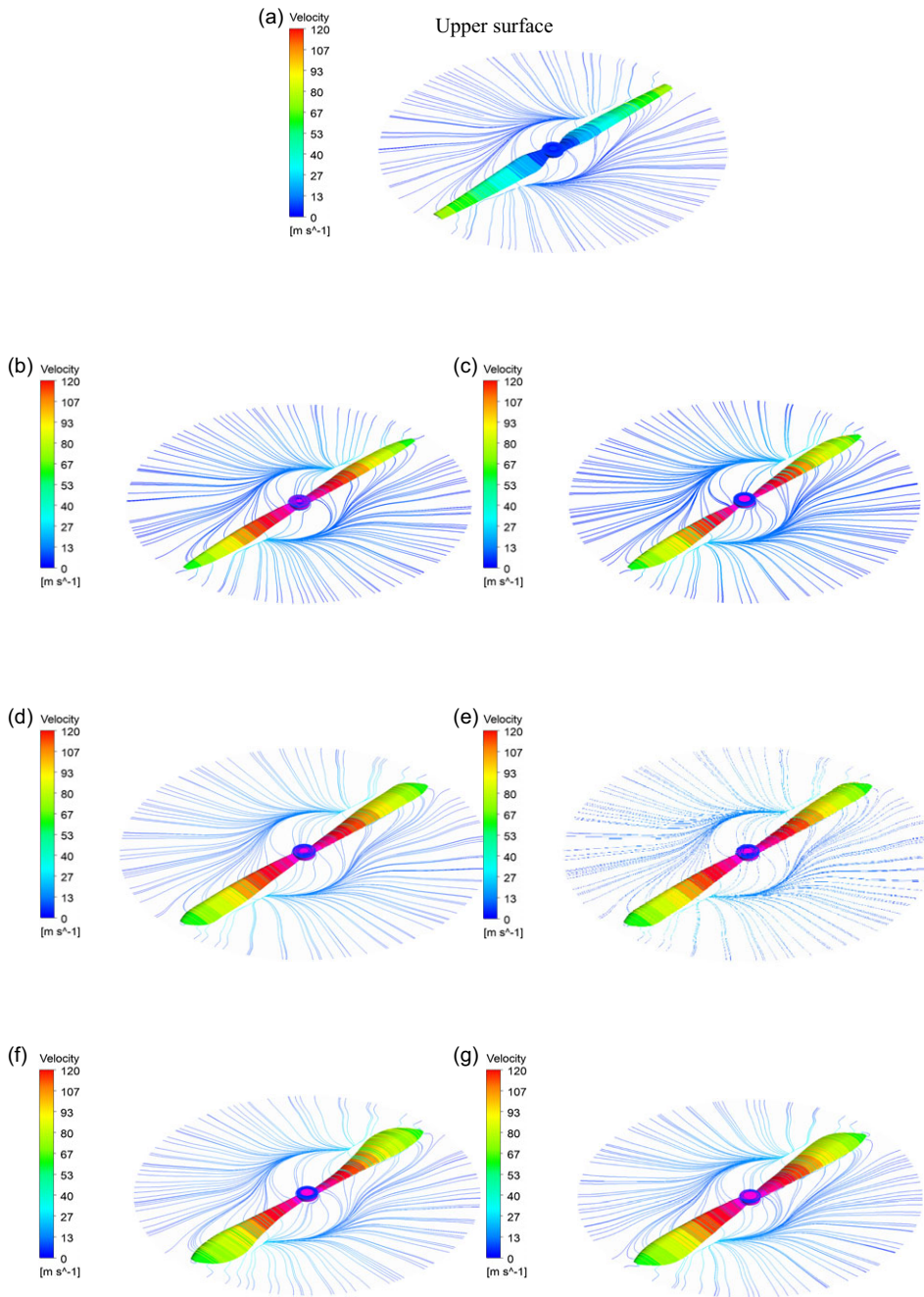


**Figure 14.** Streamlines of base propeller (a), *Mantodea* (b), *Neuroptera* (c), *Orthoptera* (d), *Odonata* (e), *Hymenoptera* (f), *Hemiptera* (g).

of mechanical power and torque coefficient across all rotational speeds. The Orthoptera propeller, having a mid-range chord distribution—neither wide nor narrow—naturally falls between these two cases. As a result, it exhibits intermediate values of mechanical power and torque coefficient, with moderate changes as rotational speed increases, paralleling its thrust and thrust coefficient behavior.

Based on relation (1), it can be inferred that an increase in the required mechanical power leads to a reduction in the propeller efficiency. In simpler terms, when the required mechanical power is increased,

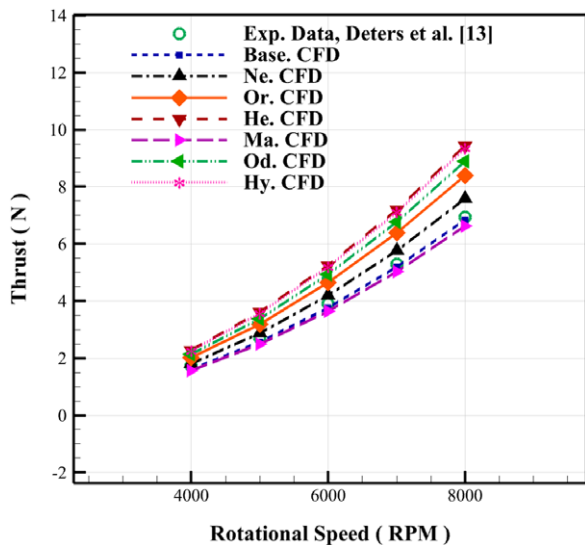


**Figure 15.** Thrust versus rotational speed for all propellers.

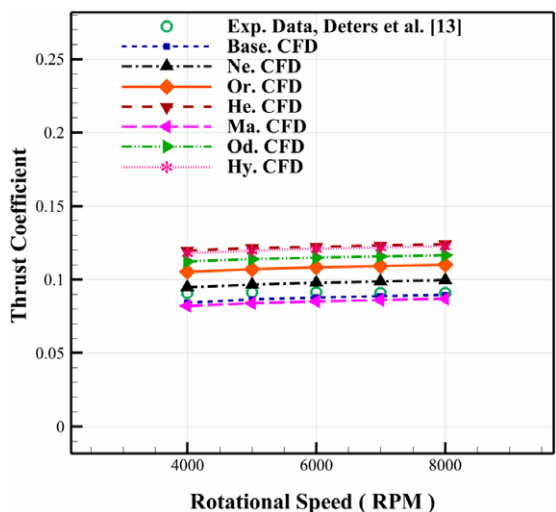


**Figure 16.** Thrust coefficient versus rotational speed for all propellers.

more energy (in the form of battery or fuel consumption) is needed for operation, which is undesirable from the propulsion efficiency perspective.

In this research, we calculated the propeller efficiency for all propellers at a range of rotational speeds. Figure 19, displays the trend of propeller efficiency as the rotational speed increases. Since the free-stream velocity is nearly zero, the propeller efficiency remains only marginally higher than zero, indicating very low performance for all propellers. It is observed that the propeller efficiency decreases as the rotational speed increases for all propellers. Wider propellers require more mechanical power for rotation, result in an increase in the required mechanical power with increasing the rotational speed. Consequently, despite the higher thrust generated by the Hemiptera-inspired propeller due to its wider blade design, its efficiency remains low. The same applies to Hymenoptera and Odonata inspired propellers. In contrast, propellers with narrower blades, like Neuroptera and Mantodea, exhibit lower propeller efficiencies. Figure 17 also highlights that, in terms of propeller efficiency,

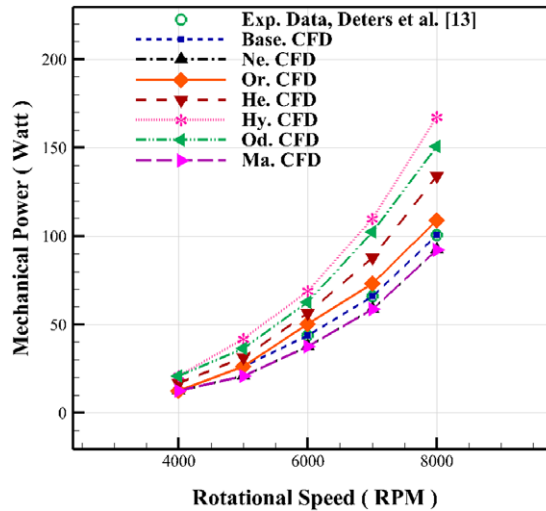


Figure 17. Mechanical power versus rotational speed for all propellers.

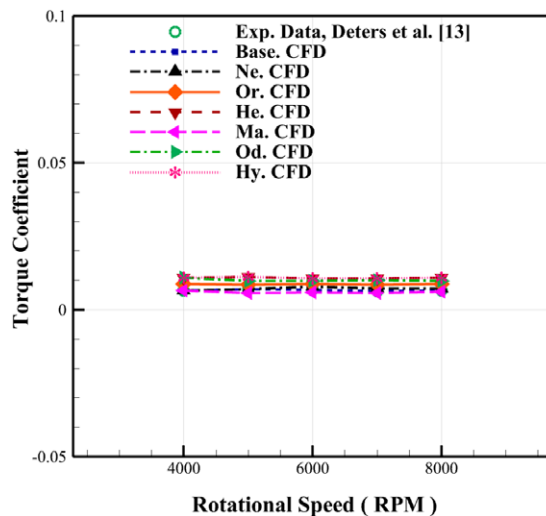


Figure 18. Torque coefficient vs rotational speed for all propellers.

Orthoptera propeller demonstrates a moderate behaviour with increasing rotational speed compared to other propellers.

Eliminating the rotational speed (horizontal axis) from the Figs 17 and 19, the variations of the required mechanical power versus variations in the propeller efficiency are obtained for all propellers that are shown in Fig. 20. It is a performance curve for the propeller that represents the variation of two performance parameters simultaneously. As is evident, there is an inverse relationship between the propeller efficiency and required mechanical power in Fig. 18. With the increase of the mechanical power, the propeller efficiency decreases. As expected, the overall behaviour in all propellers is similar. However, the rate of these trends is different.

To analyse the results practically, it is important to consider the vehicle's capability of take-off. In order for a multi-rotor to overcome its weight, it must produce a value of normal force equal to its weight. This happens at a specific rotational speed for each propeller. However, increasing the rotational speed leads to higher battery consumption and environmental noise. Therefore, it is desired for the propeller

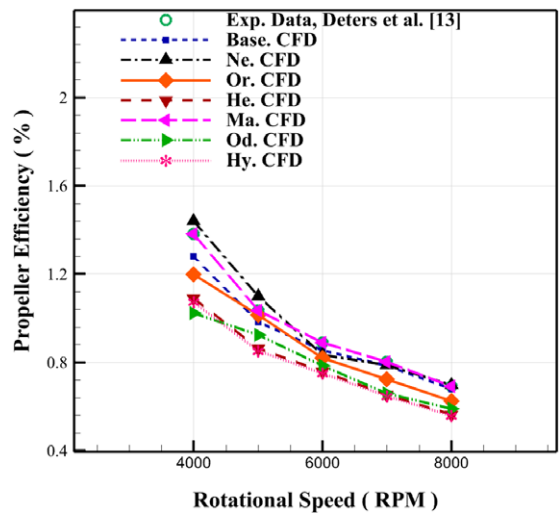


Figure 19. Propeller efficiency vs rotational speed for all propellers.

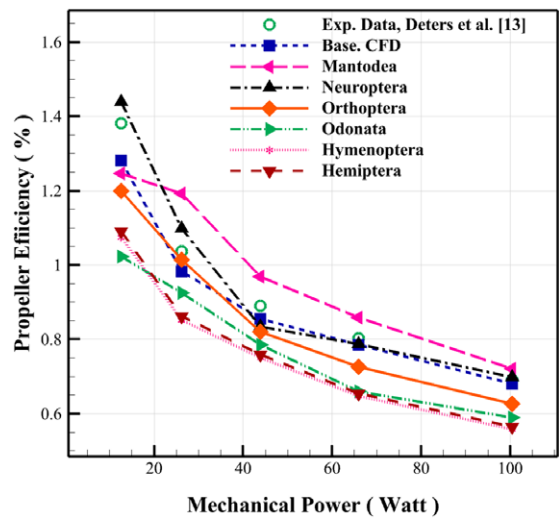
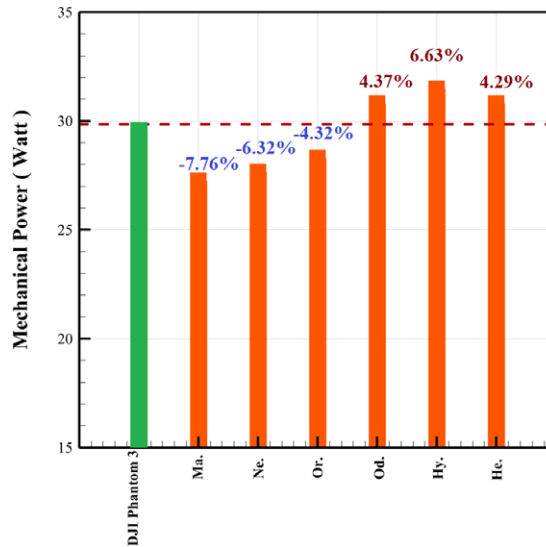


Figure 20. Propeller efficiency vs required mechanical power for all rotational speed.

to operate at a lower rotational speed, while still maintaining a constant thrust to weight ratio, such as 1:1. For a better analysis of the propeller performance, their parameters are compared at a constant thrust to weight ratio of 1:1. For this comparison, the DJI Phantom-3 drone, weighing 1.216 kg, is considered as an example. Assuming a thrust-to-weight ratio of 1:1 for take-off and considering the hovering conditions, each propeller should produce a thrust equal to 2.982 Newton. The propellers in this research are investigated at different rotational speeds and are exhibited different torque and mechanical power, as expected.

Figure 21 illustrates the values of mechanical power for all the propellers at a constant thrust to weight ratio of 1:1. Comparing the propellers reveals that their shape affects the mechanical power and the required rotational speeds for the drone to overcome its weight. In this figure, the column related to the mechanical power of the original DJI Phantom-3 propeller is highlighted in green. Additionally, a horizontal dashed line represents a baseline for comparison with the DJI Phantom-3 propeller. This figure also displays the percentage difference of each propeller compared to the DJI Phantom-3 propeller.



**Figure 21.** Mechanical power for all propellers at thrust to weight ratio of 1:1.

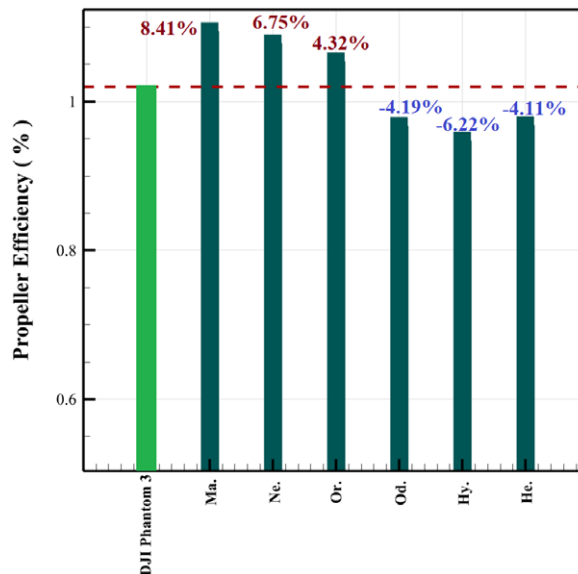


**Figure 22.** Propeller efficiency for all propellers at thrust to weight ratio of 1:1.

The propellers inspired by Odonata, Hymenoptera and Hemiptera require mechanical powers more than what is needed for the base propeller. In other words, the insect-inspired propellers having wider chord distribution requiring more mechanical power to rotate when compared to the DJI Phantom-3 propeller. Out of the six bio-inspired propellers investigated, Hymenoptera requires the most mechanical power for hovering, while Mantodea requires the least.

The amount of mechanical power needed for hovering has an impact on the propeller efficiency, as shown in Fig. 22. As mentioned earlier, an increase in required mechanical power leads to higher energy consumption (battery or fuel) during operation, which is undesirable from a propulsion efficiency perspective. This, in turn, decreases propeller efficiency (that the trend of this decrease was also illustrated in Fig. 20 for all propellers at various mechanical power). However, Mantodea, Orthoptera and

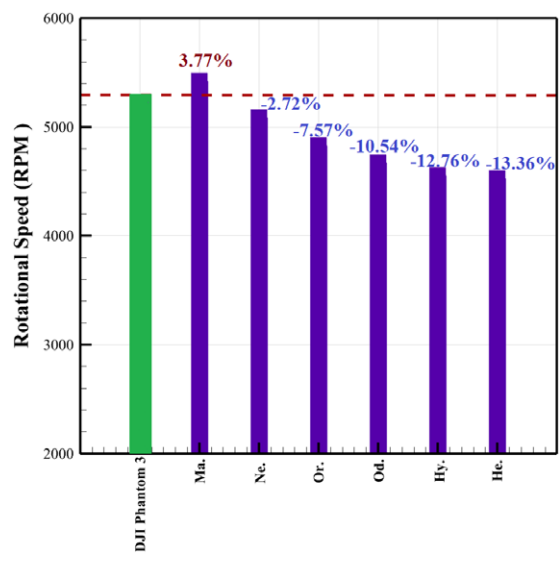


**Figure 23.** Rotational speed for all propellers at thrust to weight ratio of 1:1.

Neuroptera have higher propeller efficiency than the DJI Phantom-3 and other propellers despite their relatively narrower planforms. Mantodea exhibits the highest propeller efficiency, while Hymenoptera has the lowest.

Figure 23 demonstrates the rotational speed necessary to overcome the weight during hovering operation, with a thrust-to-weight ratio of 1:1. It is evident that all bio-inspired propellers, except for Mantodea, can achieve the required thrust at a lower rotational speed than the DJI Phantom-3 propeller. The rotational speed can be a significant factor and contribute to the noise generation and increase in noise level, and results suggest a potential correlation between reducing rotational speed and a slight decrease in noise. However, confirming this relationship would require calculations of flow-induced noise, which are outside the scope of this research. Among the propellers tested, Mantodea possesses the highest rotational speed, whereas Hemiptera has the lowest.

Finally, an abstract of the previous results about the performance parametric study on the present insect-inspired propellers is collected and presented in the Table 5. As can be seen from Table 5(a), the Hemiptera-inspired propeller has the best performance in terms of thrust and torque in all rotational speeds, but the best performance in terms of propeller efficiency and mechanical power is the Mantodea-inspired propeller. In addition, as is seen in Table 5(b), in the thrust-to-weight ratio of 1:1 (hovering condition), the Hemiptera-inspired propeller has the best performance in terms of rotational speed (minimum rotational speed), the Mantodea-inspired propeller shows better performance in terms of propeller efficiency and mechanical power.

### 6.0 Conclusion

In this study, numerical analyses were carried out to examine the aerodynamic performance of several bio-inspired propellers across a range of rotational speeds from 0 to 6,000 rpm. To validate the accuracy of our simulations, the results were compared with experimental data [13] for the DJI Phantom-3 propeller, which served as the baseline propeller. The key findings from these simulations are as follows:

- All insect-inspired propellers, except for Mantodea propeller, demonstrated higher thrust and torque compared to the DJI Phantom-3 propeller.
- An increase in rotational speed led to a decline in propeller efficiency.



**Table 5.** Highlights of the results of a performance study on the present insect-inspired propellers**a) Best Improvement Compared to DJI Phantom-3 Propeller**

Rotational speed	Thrust	Torque	Propeller efficiency	Mechanical power
4,000	Hemiptera (+31.66%)	Hemiptera (+66.66 %)	Neuroptera (+7.69 %)	Mantodea(0)
5,000	Hemiptera (+33.13 %)	Hemiptera (+60 %)	Mantodea (+6.80 %)	Mantodea (−19.99 %)
6,000	Hemiptera (+34 %)	Hemiptera (+57.14 %)	Mantodea (+7.87 %)	Mantodea (−14.29 %)
7,000	Hemiptera (+35.91 %)	Hemiptera (+66.66 %)	Mantodea (+6.25 %)	Mantodea (−11.10 %)
8,000	Hemiptera (+36.21 %)	Hemiptera (+66.66 %)	Mantodea (+2.9 %)	Mantodea (−8.33 %)

**b) Best Improvement Compared to DJI Phantom-3 Propeller in Thrust to Weight Ratio of 1:1 (Hovering Condition)**

Rotational speed	Propeller efficiency	Mechanical power
Hemiptera (−13.36%)	Mantodea (+8.41%)	Mantodea (−7.76%)

- The “**Mantodea**” propeller achieved the highest efficiency, with an 8.41% improvement over the DJI Phantom-3.
- When considering the mechanical power required, “**Mantodea**” propeller also outperformed the baseline propeller with a 7.76% reduction in power consumption.
- In terms of rotational speed, the “**Hemiptera**” propeller showed better performance by rotating 13.36% more slowly than the DJI Phantom-3.
- Based on propeller efficiency and mechanical power requirements, the “**Mantodea**” propeller exhibits acceptable performance and could be a suitable replacement for the DJI Phantom-3 propeller.
- Taking all performance parameters into account, the “**Orthoptera**” propeller displayed moderate performance.

These results suggest that bio-inspired propellers, particularly “**Mantodea-inspired propeller**” has optimal and suitable performance in terms of two parameters and, in terms of shape, is also close to the DJI Phantom-3 propeller, therefore it can be a suitable alternative. Then, by comparing the figures, it can be seen that the “**Orthoptera-inspired propeller**” is also a suitable blade and is in balance in terms of the parameters examined.

One of the key achievements of this study is the presentation of bio-inspiration (regarding insects in the present study) as a potential approach for improving aerodynamic performance. The results suggest that the present insect-inspired propellers have the potential to replace conventional propellers like the DJI Phantom-3. However, further investigations and more accurate calculations are necessary to determine the best selection. Overall, this research highlights the promising applications of bio-inspired propellers and underscores the need for in-depth studies, comprehensive analyses and experimental tests to fully harness their benefits.

**Competing interests.** The authors declare that they have no significant competing financial, professional or personal interests that might have influenced the performance or presentation of the work described in this manuscript.

**Data availability.** The data that support the findings of this study are available on reasonable request from the corresponding author.

**Funding.** This research received no specific grant from any funding agency in the public, commercial or not-for-profit sectors.

**Authors contributions.** R. Askari and M. Masdari conceived of the presented idea and supervision of the present research. Y. Zakeri Nazar contributed to the design, modeling of propeller geometries and implementation of the research, to the analysis of the results. Y. Zakeri Nazar, R. Askari and M. Masdari contributed to the writing of the manuscript.

**Acknowledgements.** This research received no special support other than the contributions of the authors, which need to be acknowledged.

## References

- [1] Mohamed, N., Al-Jaroodi, J., Jawhar, I., Idries, A. and Mohammed, F. Unmanned aerial vehicles applications in future smart cities, *Technol. Forecast. Soc. Change*, 2018, **153**, p 119293. <https://doi.org/10.1016/j.techfore.2018.05.004>
- [2] Sapit, A., Faiz Masjan, M. and Kariem Shater, S. Aerodynamics drone propeller analysis by using computational fluid dynamics, *J. Compl. Flow*, 2021, **3**, pp 12–16.
- [3] Deters, R.W., Ananda Krishnan, G.K. and Selig, M.S. Reynolds number effects on the performance of small-scale propellers, In 32nd AIAA Applied Aerodynamics Conference, 2014 <https://doi.org/10.2514/6.2014-2151>
- [4] Ramasamy, M., Johnson, B. and Leishman, J.G. Understanding the aerodynamic efficiency of a hovering micro-robot, *J. Amer. Helicop. Soc.*, 2008, **53**, pp 412. <https://doi.org/10.4050/jahs.53.412>
- [5] Yilmaz, E. and Hu, J. CFD study of quadcopter aerodynamics at static thrust conditions, 2018.
- [6] Hassanalain, M., Radmanesh, M. and Sedaghat, A. Increasing flight endurance of MAVs using multiple quantum well solar cells, *Int. J. Aeronaut. Space Sci.*, 2014, **15**, pp 212–217. <https://doi.org/10.5139/ijass.2014.15.2.212>
- [7] Schömann, J. Hybrid-electric propulsion systems for small unmanned aircraft, 2014.
- [8] Bohorquez, F., Samuel, P., Sirohi, J., Pines, D., Rudd, L. and Perel, R. Design, analysis and hover performance of a rotary wing micro air vehicle, *J. Amer. Helicop. Soc.*, 2003, **48**, pp 80. <https://doi.org/10.4050/jahs.48.80>
- [9] Ramasamy, M., Lee, T.J. and Gordon Leishman, J. Flowfield of a rotating-wing micro air vehicle, *J. Aircr.*, 2012, **44**, pp 1236–1244. <https://doi.org/10.2514/1.26415>
- [10] Brandt, J. and Selig, M. Propeller performance data at low reynolds numbers, In 49th AIAA Aerospace Sciences Meeting Including the New Horizons Forum and Aerospace Exposition, 2011. <https://doi.org/10.2514/6.2011-1255>
- [11] Jordan, W., Deters, R.W. and Narsipur, S. Aerodynamic and aeroacoustic performance of small UAV propellers in static conditions, In AIAA AVIATION 2020 FORUM, 2020. <https://doi.org/10.2514/6.2020-2595>
- [12] Shams din, S.S. and Madzni, M.Z. Aerodynamic analysis of quadrotor UAV propeller using computational fluid dynamic, *J. Compl. Flow*, 2021, **3**, pp 28–32.
- [13] Deters, R., Kleinke, S. and Selig, M. Static testing of propulsion elements for small multirotor unmanned aerial vehicles, 2017. <https://doi.org/10.2514/6.2017-3743>
- [14] Hintz, C., Khanbolouki, P., Perez, A.M., Tehrani, M. and Poroseva, S. Experimental study of the effects of bio-inspired blades and 3D printing on the performance of a small propeller, In 2018 Applied Aerodynamics Conference, 2018. <https://doi.org/10.2514/6.2018-3645>
- [15] Gomez, S., Gilkey, L.N., Kaiser, B. and Poroseva, S.V. Computational analysis of a tip vortex structure shed from a bio-inspired blade, 2014. <https://doi.org/10.2514/6.2014-3253>
- [16] Ning, Z., and Hu, H. An experimental study on the aerodynamic and aeroacoustic performances of a bio-inspired UAV propeller, In 35th AIAA Applied Aerodynamics Conference, 2017. <https://doi.org/10.2514/6.2017-3747>
- [17] Ikeda, T., Ueda, T., Nakata, T., Noda, R., Tanaka, H., Fujii, T. and Liu, H. Morphology effects of leadingedge serrations on aerodynamic force production: An integrated study using PIV and force measurements, *J. Bionic Eng.*, 2018, **15**, pp 661–672. <https://doi.org/10.1007/s4223501800544>
- [18] Wei, Y., Xu, F., Bian, S. and Kong, D. Noise reduction of UAV using biomimetic propellers with varied morphologies leading-edge serration, *J. Bionic Eng.*, 2020, **17**, pp 767–779. <https://doi.org/10.1007/s42235-020-0054-z>
- [19] Mozafari, M. and Masdari, M. Owl aeroacoustics: Analysis of a silent flight (In Persian), *J. Sharif: Mech. Eng.*, 2023, **140**, (3), pp 99–118. <https://doi.org/10.24200/j40.2022.60494.1643>
- [20] Moslem, F., Masdari, M., Fedir, K. and Moslem, B. Experimental investigation into the aerodynamic and aeroacoustic performance of bioinspired small-scale propeller planforms, *Proceedings Inst. Mech. Eng. Part G: J. Aerosp. Eng.*, 2022, **237**, pp 75–90. <https://doi.org/10.1177/09544100221091322>
- [21] Loureiro, E.V., Oliveira, N.L., Hallak, P.H., de Souza Bastos, F., Rocha, L.M., Delmonte, R.G.P. and de Castro Lemonge, A.C. Evaluation of low fidelity and CFD methods for the aerodynamic performance of a small propeller, *Aerosp. Sci. Technol.*, 2021, **108**, p 106402. <https://doi.org/10.1016/j.ast.2020.106402>
- [22] Chevula, S., Chillamcharal, S. and Maddula, S.P. A computational design analysis of UAV's rotor blade in low-temperature conditions for the defence applications, *Int. J. Aerosp. Eng.*, 2021, **2021**, p e8843453. <https://doi.org/10.1155/2021/8843453>
- [23] Varki, M., Yeter, E. and Doğru, M.H. Effect of propellers numbers and horizontal distance in design of VTOL. *Int. J. Mater. Eng Technol.*, 2022, **5**, pp 23–27.
- [24] Mahmuddin, F. Rotor blade performance analysis with blade element momentum theory, *Energy Procedia.*, 2017, **105**, pp 1123–1129. <https://doi.org/10.1016/j.egypro.2017.03.477>
- [25] DJI Team, “phantom-3-standard,” DJI. <https://www.dji.com> (accessed 2021).

- [26] “Phantom-3 Standard - User Manual V 1.4,” Sep. 01, 2015.
- [27] Samways, M. and Deacon, C. Extinction reprieve for the ancient and imperiled dragonflies at the southern tip of Africa, 2021. <https://doi.org/10.1016/B978-0-12-821139-7.00047-7>
- [28] Flindt, R. and Springerlink. *Online Service, Amazing Numbers in Biology*. Springer Berlin Heidelberg, Berlin, Heidelberg, 2006.
- [29] Gibb, T. Contemporary insect diagnostics: The art and science of practical entomology, In *Contemporary Insect Diagnostics: The Art and Science of Practical Entomology*, 2014, pp 1–336.
- [30] Liu, D., Hefler, C., Shyy, W. and Qiu, H. Implications of dragonfly’s muscle control on flapping kinematics and aerodynamics, *Phys Fluids (1994)*, 2022, **34**, p 081902. <https://doi.org/10.1063/5.0097790>
- [31] Chitsaz, N., Siddiqui, K., Marian, R. and Chahl, J. An experimental study of the aerodynamics of micro corrugated wings at low Reynolds number, *Exp. Therm Fluid Sci.*, 2021, **121**, p 110286. <https://doi.org/10.1016/j.expthermflusci.2020.110286>
- [32] Ogunwa, T., Abdullah, E. and Chahl, J. Modeling and control of an articulated multibody aircraft, *Appl. Sci.*, 2022, **12**, p 1162. <https://doi.org/10.3390/app12031162>
- [33] Outomuro, D., Adams, D.C. and Johansson, F. Wing shape allometry and aerodynamics in calopterygid damselflies: a comparative approach, *BMC Evol. Biol.*, 2013, **13**, p 118. <https://doi.org/10.1186/1471214813118>
- [34] Wootton, R. Dragonfly flight: Morphology, performance and behaviour. *Int. J. Odonatol.*, 2020, **23**, pp 31–39. <https://doi.org/10.1080/13887890.2019.1687991>
- [35] Norberg, R.Å. Hovering Flight of the Dragonfly *Aeschna Juncea* L., Kinematics and Aerodynamics. In Wu, T.Y.T., Brokaw, C.J., Brennen, C. (eds), *Swimming and Flying in Nature*. Springer, 1975, Boston, MA, pp 763–781. [https://doi.org/10.1007/978-1-4757-1326-8\\_19](https://doi.org/10.1007/978-1-4757-1326-8_19)
- [36] Vance, J. Experimental and natural variation in hovering flight capacity in bees, Hymenoptera: Apidae, 2009. <https://doi.org/10.34917/1354557>
- [37] Belyaev, O.A. and Farisenkov, S.E. A study on allometry of wing shape and venation in insects. Part 1. Hymenoptera, *Mosc. Univ. Biol. Sci. Bull.*, 2018, **73**, pp 229–235. <https://doi.org/10.3103/s0096392518040028>
- [38] Dudley, R. and Ellington, C.P. Mechanics of forward flight in bumblebees: II. Quasi-steady lift and power requirements, *J. Exp. Biol.*, 1990, **148**, pp 53–88. <https://doi.org/10.1242/jeb.148.1.53>
- [39] Golding, Y.C., Ennos, A.R. and Edmunds, M. Similarity in flight behaviour between the honeybee *Apis mellifera* (Hymenoptera: apidae) and its presumed mimic, the dronefly *Eristalis tenax* (Diptera: syrphidae), *J. Exp. Biol.*, 2001, **204**, 139–145. <https://doi.org/10.1242/jeb.204.1.139>
- [40] Zakeri Nazar, Y., Askari, R. and Masdari, M. Numerical simulation and aerodynamic analysis of insect-inspired propeller planforms, Master Thesis, University of Tehran, 2023, pp 30–35.
- [41] Zakeri Nazar, Y., Askari, R. and Masdari, M. Enhancement of aerodynamic efficiency in a commercial propeller through bio-inspired blade design, *Int. J. Mod. Phys. C.*, 2025. <https://doi.org/10.1142/s0129183125500809>
- [42] Ábrahám, L. A new Creoleon sp. n. (Neuroptera: Myrmeleontidae) from Socotra (Yemen), *Nat. Somogy.*, 2020, **35**, pp 37–44. <https://doi.org/10.24394/natsom.2020.35.37>
- [43] Hectonichus, Pyrgomorphidae - Phymateus karschi [Is licensed under CC BY-SA 3.0]. <https://creativecommons.org/licenses/by-sa/3.0/?ref=openverse>
- [44] Constant, J. and Pham, T. Review of the clavatus group of the lanternfly genus *Pyrops* (Hemiptera: Fulgoromorpha: Fulgoridae), *Eur. J. Taxon.*, 2017, **305**, pp 1–26. <https://doi.org/10.5852/ejt.2017.305>
- [45] Descouens, D. File: Raptrix perspicua MHNT male.jpg [Is licensed under CC BY-SA 3.0]. <https://creativecommons.org/licenses/by-sa/3.0/?ref=openverse>
- [46] Seehausen, M. New to the fauna of Hong Kong: Matrona basilaris Selys, 1853 (Odonata: Calopterygidae), *IDFRep.*, 2014, **65**, pp 3–5.
- [47] Anderson, J.D. Computational Fluid Dynamics. The basics with applications, McGraw-Hill, 1995.
- [48] GarofanoSoldado, A., SanchezCuevas, P.J., Heredia, G. and Ollero, A. Numerical experimental evaluation and modelling of aerodynamic ground effect for smallscale tilted propellers at low reynolds numbers, *Aerosp. Sci. Technol.*, 2022, **126**, pp 107625. <https://doi.org/10.1016/j.ast.2022.107625>
- [49] Andersson, B., Andersson, R., Håkansson, L., Mortensen, M., Sudiyo, R. and van Wachem, B. *Computational Fluid Dynamics for Engineers*. Cambridge University Press, 2011, Cambridge.
- [50] Ansys® Fluent, Release 2021 R1, Help System, Ansys Fluent Theory Guide, ANSYS, Inc.
- [51] Garofano-Soldado, A., Sanchez-Cuevas, P.J., Heredia, G. and Ollero, A. Numerical-experimental evaluation and modelling of aerodynamic ground effect for small-scale tilted propellers at low reynolds numbers, *Aerosp. Sci. Technol.*, 2022, **126**, p 107625. <https://doi.org/10.1016/j.ast.2022.107625>
- [52] Han, H., Xiang, C., Xu, B. and Yu, Y. Aerodynamic performance and analysis of a hovering micro-scale shrouded rotor in confined environment, *Advances Mech. Eng.*, 2019, **11**, p 168781401882332. <https://doi.org/10.1177/1687814018823327>
- [53] Lopez, O.R., Escobar, J. and Pociña Pérez, A. Computational study of the wake of a quadcopter propeller in Hover, 2017. <https://doi.org/10.2514/6.2017-3961>
- [54] Kutty, H. and Rajendran, P. 3D CFD simulation and experimental validation of small APC slow flyer propeller blade, *Aerospace*, 2017, **4**, p 10. <https://doi.org/10.3390/aerospace4010010>
- [55] Schetz, J.A. and Bowersox, R.D.W. Boundary Layer Analysis. American Institute of Aeronautics and Astronautics, Reston, Va, 2012. <https://doi.org/10.2514/4.868245>

- [56] Li, Y., Yonezawa, K., Xu, R. and Liu, H. A biomimetic rotor-configuration design for optimal aerodynamic performance in quadrotor drone, *J. Bionic Eng.*, 2021, **18**, pp 824–839. <https://doi.org/10.1007/s42235-021-0069-0>
- [57] Wilcox, D.C. Formulation of the k-w turbulence model revisited, *AIAA J.*, 2008, **46**, pp 2823–2838. <https://doi.org/10.2514/1.36541>
- [58] Menter, F. Zonal two equation K-W turbulence models for aerodynamic flows. In 23rd Fluid Dynamics, Plasmadynamics, and Lasers Conference, 1993. <https://doi.org/10.2514/6.1993-2906>